Received: 24 October 2023 | Revised: 16 January 2024 | Accepted: 17 January 2024

DOI: 10.1002/pro.4915

RESEARCH ARTICLE

THE PROTEIN SOCIETY WILEY

Crystal structure of the tegument protein UL82 (pp71) from human cytomegalovirus

Jan Eberhage[1,2] | **Ian P. Bresch**[1,2] | **Ramya Ramani**[3,4] | **Niklas Viohl**[1,2] | **Thalea Buchta**[3] | **Christopher L. Rehfeld**[1,2] | **Petra Hinse**[1] | **Thomas F. Reubold**[1] | **Melanie M. Brinkmann**[3,4] | **Susanne Eschenburg**[1,2]

[1]Institute for Biophysical Chemistry, Hannover Medical School, Hannover, Germany

[2]Cluster of Excellence RESIST (EXC 2155), Hannover Medical School, Hannover, Germany

[3]Institute of Genetics, Technische Universität Braunschweig, Germany

[4]Virology and Innate Immunity Research Group, Helmholtz Centre for Infection Research (HZI), Braunschweig, Germany

Correspondence
Melanie M. Brinkmann, Institute of Genetics, Technische Universität Braunschweig, 38106 Braunschweig, Germany.
Email: m.brinkmann@tu-braunschweig.de

Susanne Eschenburg, Institute for Biophysical Chemistry, Hannover Medical School, Carl-Neuberg-Straße 1, 30625 Hannover, Germany.
Email: eschenburg.susanne@mh-hannover.de

Funding information
Life Science Foundation; Deutsche Forschungsgemeinschaft

Review Editor: Jeanine Amacher

Abstract

Human cytomegalovirus (HCMV) is an opportunistic pathogen that infects a majority of the world population. It may cause severe disease in immunocompromised people and lead to pregnancy loss or grave disabilities of the fetus upon congenital infection. For effective replication and lifelong persistence in its host, HCMV relies on diverse functions of its tegument protein UL82, also known as pp71. Up to now, little is known about the molecular mechanisms underlying the multiple functions of this crucial viral protein. Here, we describe the X-ray structure of full-length UL82 to a resolution of 2.7 Å. A single polypeptide chain of 559 amino acids mainly folds into three ß-barrels. We show that UL82 forms a dimer in the crystal as well as in solution. We identify point mutations that disturb the dimerization interface and show that the mutant protein is monomeric in solution and upon expression in human cells. On the basis of the three-dimensional structure, we identify structural homologs of UL82 from other herpesviruses and analyze whether their functions are preserved in UL82. We demonstrate that UL82, despite its structural homology to viral deoxyuridinetriphosphatases (dUTPases), does not possess dUTPase activity. Prompted by the structural homology of UL82 to the ORF10 protein of murine herpesvirus 68 (MHV68), which is known to interact with the RNA export factor ribonucleic acid export 1 (Rae1), we performed coimmunoprecipitations and demonstrated that UL82 indeed interacts with Rae1. This suggests that HCMV UL82 may play a role in mRNA export from the nucleus similar to ORF10 encoded by the gammaherpesviruses MHV68.

KEYWORDS

crystal structure, cytomegalovirus, HCMV, herpesvirus, immune response, KSHV, MHV68, ORF10, pp71, Rae1, UL82

Jan Eberhage and Ian P. Bresch contributed equally to this work.

1 | INTRODUCTION

Human cytomegalovirus (HCMV) is an opportunistic betaherpesvirus, which has adapted well to its human host. During coevolution, HCMV has developed a multitude of strategies to evade the host's immune response, thereby allowing the establishment of latency and lifelong infections (Berry et al., 2020; Griffiths & Reeves, 2021). HCMV is widespread with an estimated seroprevalence of over 60% in the European population and over 90% in many developing countries (Zuhair et al., 2019). Although HCMV infection of healthy individuals is usually subclinical, life-threatening HCMV disease is frequent among the immunocompromised (Griffiths & Reeves, 2021). Viral reactivation in organ recipients, HIV-infected patients, or cancer patients undergoing aggressive chemotherapy may lead to viremia, end-stage organ failure, or donor organ rejection (Azevedo et al., 2015; Cho et al., 2019; Razonable & Humar, 2019; Yang et al., 2020). Worldwide, HCMV infection in utero is the most common congenital viral infection, and the leading infectious cause of birth defects such as mental retardation and hearing loss (Coppola et al., 2019; Dietrich & Schieffelin, 2019; Fowler & Boppana, 2018; Goderis et al., 2014; Njue et al., 2020; Rawlinson et al., 2017).

HCMV is a large and highly complex DNA virus, with a genome comprising more than 230 kbp and encoding more than 200 open reading frames (ORFs), making it one of the largest viruses that infect mammals (Davison et al., 2003; Gatherer et al., 2011; Stern-Ginossar et al., 2012). Like all herpesviruses, the HCMV virion possesses a proteinaceous matrix called tegument between the viral nucleocapsid and the lipid envelope, which contains proteins of viral and cellular origin (Bogdanow et al., 2023; Varnum et al., 2004; Yu et al., 2011). Upon infection, the tegument proteins are delivered into the host cell and mediate important functions, such as initiation of viral gene expression or manipulation of the cellular intrinsic and innate immune responses, before they are de novo transcribed and translated and eventually packaged into newly formed virions (Kalejta, 2008).

The HCMV tegument protein phosphoprotein 71, either named pp71 after its molecular weight or, alternatively, named UL82 after its encoding ORF located in the unique long (UL) region of the HCMV genome, is critical for efficient HCMV replication, as viruses lacking this protein have severe growth defects (Dunn et al., 2003; D. Yu et al., 2003). HCMV pp71/UL82, hereafter referred to as UL82, plays a plethora of roles during HCMV infection. Studies have demonstrated UL82 to interact with retinoblastoma proteins via its conserved motif ^{216}LxCxD^{220} (Kalejta et al., 2003; Kalejta & Shenk, 2003a, 2003b) and with death-associated protein 6 (DAXX) (Hofmann et al., 2002; Nobre et al., 2019), which mediates degradation of these transcriptional repressors (Hwang & Kalejta, 2007; Kalejta, 2004) and allows the virus to establish a subcellular environment conducive for viral replication (Saffert & Kalejta, 2006). UL82's ability to target DAXX, a component of promyelocytic leukemia protein nuclear bodies, is crucial to prevent transcriptional silencing of the viral genome (Hofmann et al., 2002; Hwang & Kalejta, 2007; Saffert & Kalejta, 2006, 2007). Furthermore, UL82 was shown to manipulate the cellular antiviral immune response. Regarding the innate type I interferon (IFN) response, UL82 antagonizes the cGAS (cyclic GMP–AMP synthase)-STING (stimulator of interferon genes) signaling pathway, presumably through inhibition of STING trafficking and subsequent recruitment of TBK1 (TANK-binding kinase 1) and the transcription factor IRF3, which poses a prerequisite for STING's ability to induce transcription of type I IFNs (Fu et al., 2017; Nukui et al., 2020). UL82 also seems to target the adaptive immune response by mediating the downregulation of MHC class I cell surface expression by a yet unknown mechanism (Trgovcich et al., 2006). UL82 was shown to interact with two other tegument proteins of HCMV, UL35, and UL32 (Bogdanow et al., 2023; Nobre et al., 2019; Phillips & Bresnahan, 2011; Schierling et al., 2004; To et al., 2011). Several further cellular proteins were identified in a proteomics study as UL82 interaction partners (Nobre et al., 2019), and UL82 was also described to bind viral and cellular RNA (Lenarcic et al., 2015), but the functional consequences of these putative interactions are not yet clear.

Up to now, only little is known about the underlying molecular mechanisms by which UL82 fulfills its diverse functions. Here, we have determined the high-resolution crystal structure of full-length UL82. On the basis of the three-dimensional structure, we have identified homologs of UL82 and provide evidence that this approach may allow novel insights into the molecular mechanisms of UL82 that enable viral persistence and replication.

2 | RESULTS

2.1 | Protein production, crystallization, and structure determination

We expressed full-length wild-type UL82 (UL82-WT) of HCMV strain AD169 fused to an N-terminal maltose-binding protein (MBP)-tag in the *Spodoptera frugiperda* cell line Sf9 using a baculovirus expression system and purified the protein to homogeneity. When we cleaved

the fusion protein with tobacco etch virus (TEV) protease at the TEV cleavage site included in the linker region connecting UL82 to the MBP-tag, UL82 showed a strong tendency to form aggregates and to precipitate. We therefore set up crystallization experiments with the intact MBP-UL82 fusion protein using different commercially available high-throughput screens and obtained crystals under several conditions. The final refined condition contained 0.1 M 2-(N-morpholino)ethanesulfonic acid (MES) (pH 6.5), 0.2 M $MgCl_2$, and 7.25% polyethylene glycole (PEG) 4000.

We solved the crystal structure of UL82 de novo using single anomalous dispersion from a mercury derivative for phasing. We refined the structure to a resolution of 2.7 Å yielding R_{work} and R_{free} values of 20.67% and 23.06%, respectively (Table 1). The crystal structure revealed a symmetric dimer in the asymmetric unit, where the protomers are related via a twofold rotation axis. Noncrystallographic symmetry restraints were applied in default mode of Phenix (Liebschner et al., 2019). The final model contains amino acid residues 13–147, 155–396, and 479–539 of protomer A of UL82, residues 10–147, 152–399, and 479–539 of protomer B of UL82, altogether 48 water molecules and one polyethylene molecule, which stems from the cryoprotectant. After refinement, the Ramachandran plot showed 95.9% of the residues to be located in the favored region, 2.8% in the allowed region, and 1.3% in the disallowed region.

Each protomer of the UL82 dimer folds into four domains (Figure 1a). Domains I, II, and III form β-barrels. Domain IV comprises a four-membered twisted antiparallel β-sheet and a fifth strand that forms an antiparallel β-sheet with one of the β-strands of domain II (Figure 1b, c). Domain I contains the N and C terminus of UL82 and harbors the only helix in the protomer. This N-terminal helix spans residues 14 to 27 and interacts with the second protomer of the UL82 dimer (Figure 2a).

TABLE 1 Data collection and refinement statistics.

	UL82
Data collection	
Space group	I 21 21 21
Cell dimensions	
a, *b*, *c* (Å)	90.61, 137.44, 275.12
α, *β*, *γ* (°)	90, 90, 90
Resolution (Å)	47.03–2.7 (2.8–2.7)[a]
$CC_{1/2}$	1 (0.793)
R_{meas}	0.07545 (1.21)
Total reflections	655,094 (67475)
Unique reflections	47,593 (4846)
Completeness (%)	99.95 (99.98)
Redundancy	13.8 (14.4)
$I/\sigma I$	22.55 (2.11)
Refinement	
Resolution range	48.61–2.7 (2.76–2.7)
R_{work}	0.2067 (0.5357)
R_{free}	0.2306 (0.5882)
No. of atoms	7057
Protein	7001
Water	43
Polyethylene glycole	13
B-factors	
Protein	81.80
Water	81.07
PEG	125.59
Root mean square (R.m.s.) deviations	
Bond lengths (Å)	0.005
Bond angles (°)	0.71
Protein data bank entry	8QDO

[a]Highest resolution shell is shown in parenthesis.

2.2 | Dimeric nature of UL82 and structural implication for a regulatory purpose

Dimerization of UL82 is achieved by interactions between domain I of one protomer and domain II of the other protomer (Figure 1b). The two main interaction interfaces are present twice due to the rotational symmetry of the dimer. Altogether, the interaction surface area between the two protomers is about 1950 $Å^2$ as determined using the Proteins, Interfaces, Strucures and Assemblies (PISA) server (Krissinel & Henrick, 2007). The amino acid residues involved in the polar or charged interactions of the first dimer interface are R31, S65, R66, D495, D496, and D522 at the top of the β-barrel of domain I and R164, A167, R173, E214, Q215, and C218 of the β-barrel of the other protomer's domain II (Figure 2a). The side chains of R31 and S65 interact with the carbonyl oxygens of C218 and Q215, respectively. D495 and D522 contribute to a network of charged interactions with R164 and R173. R66 forms a salt bridge to E214 and D496 interacts with the main-chain nitrogen of A167 (Figure 2a). The second main interaction interface involves the N-terminal helix and includes a salt bridge and a hydrogen bond between E21 of the helix and R160 and T177, respectively, of domain II of the opposing protomer (Figure 2a).

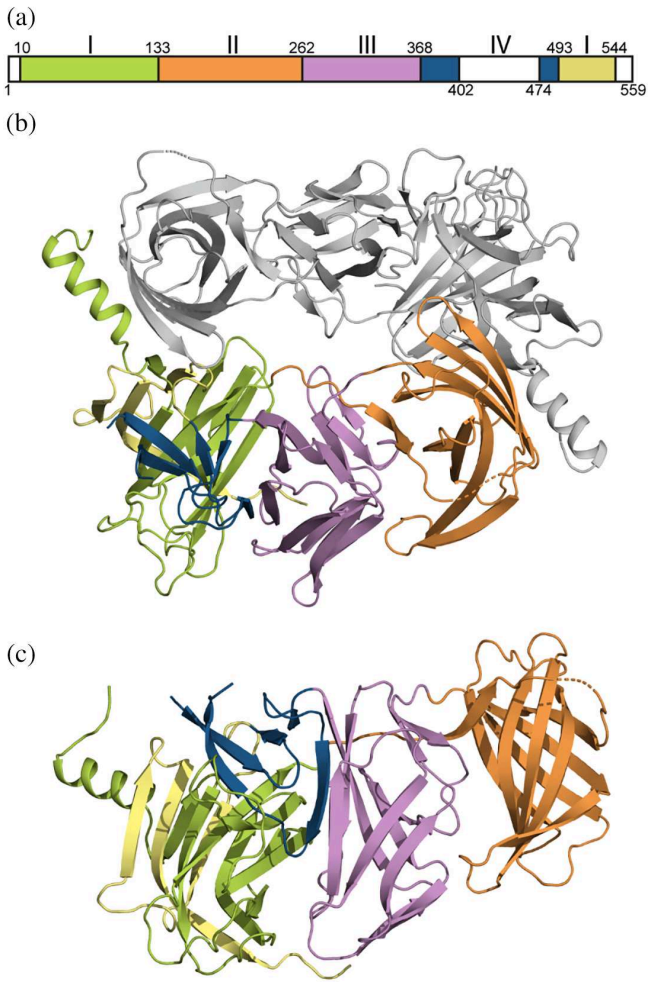

FIGURE 1 Crystal structure of UL82. (a) Domain organization of UL82. UL82 consists of four different domains (I–IV). Domain I is formed by the N- and the C-terminal region of UL82. The N-terminal part of domain I is shown in green, domain II in orange, domain III in purple, domain IV in blue, and the C-terminal part of domain I in yellow. (b) Cartoon representation of the UL82 dimer with one protomer of UL82 colored according to its domain architecture shown in (a), the second protomer is shown in gray. (c) Cartoon representation of one UL82 protomer rotated by 90° around a horizontal axis in relation to the orientation in (b).

To analyze whether the dimer seen in the crystal is also formed in solution, we subjected purified MBP-UL82-WT to analytical size exclusion chromatography (SEC) at concentrations between 1 μM and 100 μM (Figure 2b). The elution volume was independent of the protein concentration and corresponds well with a dimer of UL82. To probe the dimer interface observed in the crystal structure, we introduced the point mutations R66E and D522R into UL82 and subjected the purified MBP-UL82-R66E/D522R mutant to SEC. The mutant protein displayed a concentration-dependent transition from dimer to monomer between 1 and 100 μM (Figure 2b).

To examine whether UL82 forms dimers also in a physiological context, we expressed C-terminally myc-tagged UL82-WT or UL82-R66E/D522R, which carries the point mutations R66E and D522R, in 293 T cells. We analyzed the cell lysates by native polyacrylamide gel electrophoresis (PAGE) to separate the proteins by their size, shape, and overall bulkiness. UL82-WT migrated slower than UL82-R66E/D522R (Figure 2c), corroborating the view that UL82 exists as dimer in the cellular context and that the dimer can be disrupted into monomeric UL82 if the dimer interfaces observed in the crystal are disturbed by appropriate point mutations.

It will be interesting to see, whether the dimeric status of UL82 may have a regulatory impact on UL82's function in future experiments. Our crystal structure suggests that the subcellular localization of UL82, interference of UL82 with the cGAS-STING pathway, and a possible interaction of UL82 with retinoblastoma proteins may rely on a monomeric state of UL82. Previous studies have described an important posttranslational modification of UL82: when phosphorylated at Threonine 223 (T223), UL82, which can localize in both the cytoplasm and the nuclear compartment, does not enter the nucleus (Shen et al., 2008). Moreover, phosphorylation of T223 was also shown to be crucial for UL82's inhibitory effect on the cGAS-STING signaling pathway (Fu et al., 2017). In our crystal structure, T223 is located in a seven-membered loop (residues 217–223) connecting two β-strands of the barrel of domain II (Figure 3). The loop is oriented such that the side chain of T223 protrudes into the lumen of the β-barrel with its oxygen atom being about 5 Å away from the protein surface. This renders T223 inaccessible for phosphorylation in the observed protein conformation. The LxCxD motif (residues 216–220), which is vital for binding of retinoblastoma protein (Rb) as well as its homologs p107 and p130 (Kalejta & Shenk, 2003a), is preceding T223 and is also not accessible in the observed loop conformation (Figure 3). It was shown that the side chains of the LxCxD motif have to be solvent-exposed to bind interaction partners (Lee et al., 1998; Putta et al., 2022). As long as UL82 remains in the dimeric state, the loop cannot reorient to expose the side chains of T223 and of the LxCxD motif, suggesting that the cellular localization of UL82, its interference with the cGAS-STING pathway, and its interaction with members of the retinoblastoma protein family may rely on a monomeric state of UL82.

2.3 | Structural homology to dUTPases and dUTPase-like proteins of other herpes viruses

Our crystal structure enabled us to search for structural homologs of UL82 in the protein data bank (PDB) using the DALI server (Holm, 2022). The search revealed a

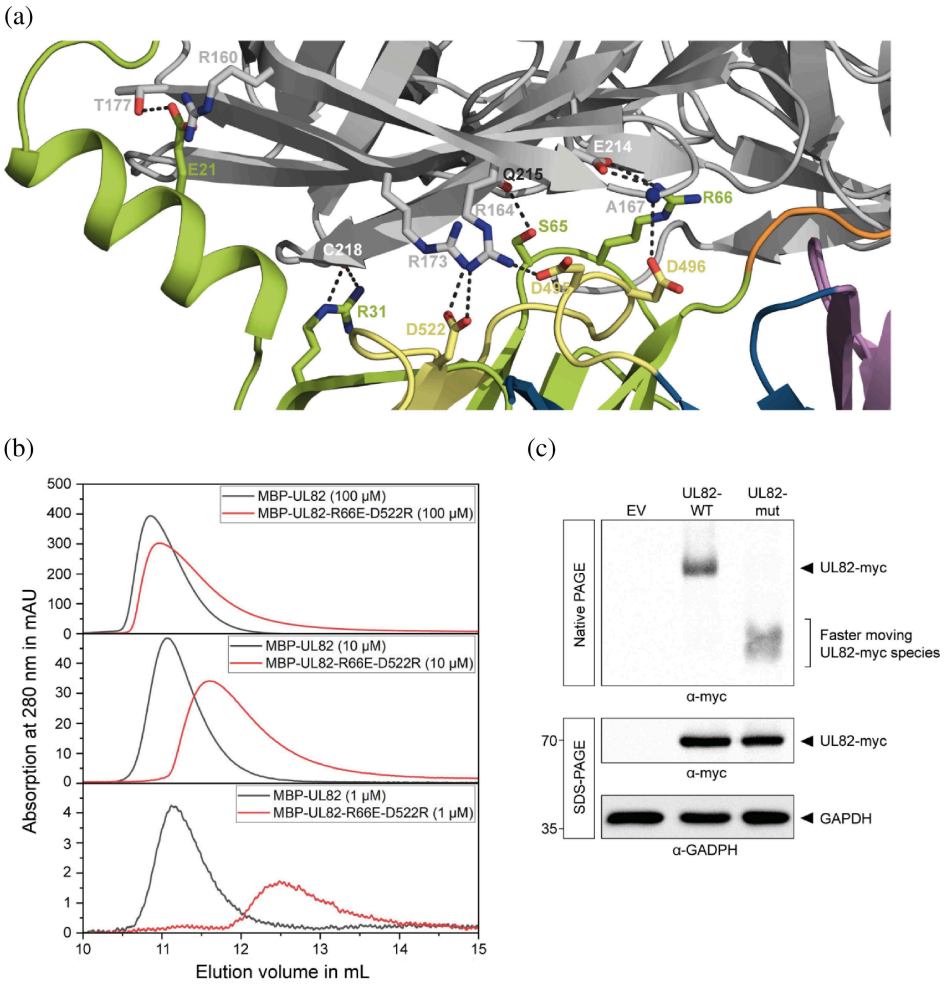

FIGURE 2 Dimeric nature of UL82 and mutational analysis. (a) Cartoon representation of the dimer interface. Color code as in Figure 1b. Interacting side chains are shown as sticks. Polar or charged interactions are delineated as dashed lines. C215 and Q218 only interact via their main-chain carbonyl oxygens. (b) Size exclusion chromatography of MBP-tagged wild-type UL82 (UL82-WT; black) and the UL82-R66E/D522R mutant (red) with three different initial concentrations. (c) Native polyacrylamide gel electrophoresis (PAGE) of UL82 wild-type (UL82-WT) and the UL82-R66E/D522R mutant (UL82-mut). 293 T cells were transfected with an empty vector (EV) or plasmids encoding C-terminally myc-tagged UL82-WT or UL82- R66E/D522R and lysed 20 h later. Lysates were subjected to native PAGE (upper panel) and SDS-PAGE (lower panel) followed by immunoblotting with anti-myc and anti-GAPDH antibodies. GADPH, glyceraldehyde-3-phosphate dehydrogenase; mut, mutant; MBP, maltose-binding protein.

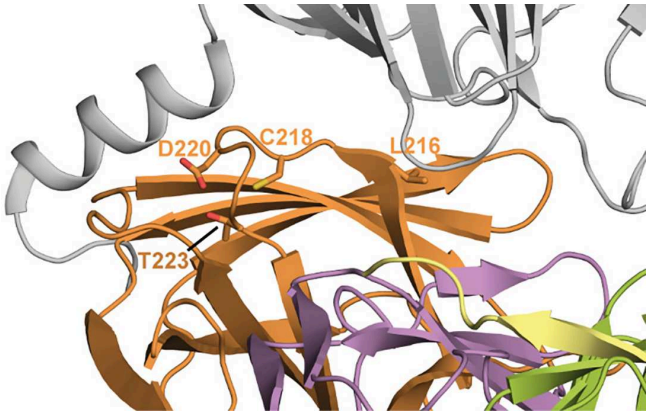

FIGURE 3 The location of the LxCxD motif and of Threonine 223 (T223) in UL82. Cartoon representation of a zoom of the UL82 dimer. Color code as in Figure 1b. Side chains are shown as stick models.

dUTPase from the gammaherpesvirus Epstein–Barr virus (EBV) named BLLF3 (Tarbouriech et al., 2005) as the closest match. Superposition of UL82 and BLLF3 via 189 structurally equivalent Cα atoms yielded a root mean square deviation of 2.74 Å (Figure 4a). Further close matches were a dUTPase from *Escherichia coli* (*E. coli*) (Cedergren-Zeppezauer et al., 1992) and ORF10 from the murine herpesvirus 68 (MHV68) (Feng et al., 2020), in the following referred to as MHV68 ORF10. dUTPases are found in numerous viruses and bacteria, where the enzymes are important for maintaining a low dUTP/dTTP ratio in the cell, thereby contributing to the integrity of the DNA (Tye et al., 1977). Evolution of dUTPases in *herpesviridae* yielded proteins that contain dUTPase domains but show no dUTPase activity at all and may excert a different function (Davison & Stow, 2005).

Comparison of the dUTP-binding site of BLLF3 with the structurally equivalent regions in UL82 suggests that UL82 should not be able to bind dUTP (Figure S1), in accordance with the crystal structure of MHV ORF68 (Feng et al., 2020). Positioning and binding of the uracil base moiety of dUTP is abrogated by a salt bridge between R93 and D100 in UL82. Moreover, the coordination of the phosphate moiety in BLLF3 is mainly achieved by charged interaction with an arginine side chain. This arginine is replaced by E321 in UL82, thus repelling the β-phosphate of dUTP. To confirm this interpretation of our structure, we spectrometrically measured

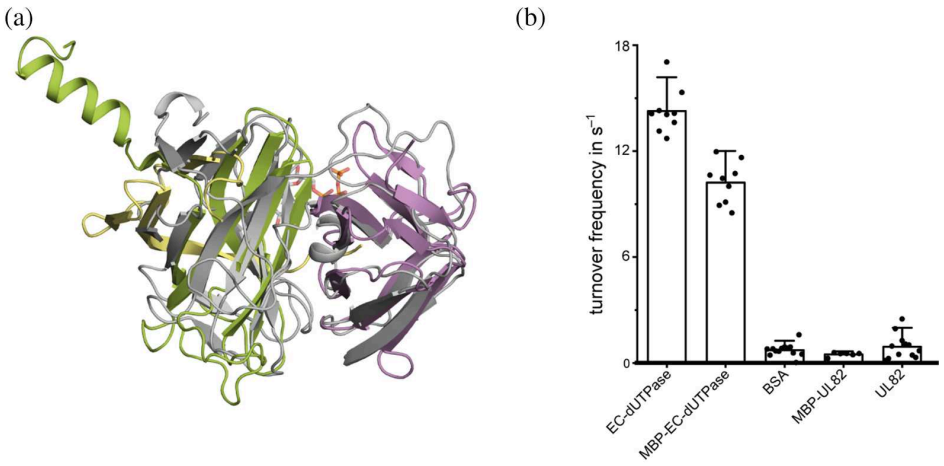

FIGURE 4 UL82 is a structural homolog of the Epstein–Barr virus (EBV)–deoxyuridinetriphosphatase (dUTPase) BLLF3 but not a functional homolog. (a) Cartoon representation of the superposition of domain I and III of a UL82 protomer with BLLF3 (PDB ID 2BT1). UL82 is colored as in Figure 1, BLLF3 is shown in gray. The α,β-imino-dUTP of BLLF3 is shown as stick model. (b) dUTPase assay. The dUTPase of *Escherichia coli* (EC) used as a positive control displays a dUTPase activity comparable to published values (Mustafi et al., 2003). Neither MBP-UL82 nor UL82 alone hydrolyze dUTP. PDB, protein data bank; BSA, bovine serum albumine; MBP, maltose binding protein.

the release of protons during hydrolysis of dUTP via the pH-dependent change of the absorption of phenol red. We found that UL82 indeed does not display discernible dUTPase activity, whereas the *E. coli*–dUTPase used as positive control hydrolyzed 14 dUTP molecules per molecule per second (Figure 4b).

MHV68 ORF10 was shown to inhibit the export of mRNA from the nucleus by binding to the ribonucleic acid export 1 (Rae1) protein and the nuclear pore protein Nup-98 (Feng et al., 2020). Given the structural homology between UL82 and MHV68 ORF10 (Figure 5a), we analyzed whether UL82 may interact with Rae1. For this purpose, we cotransfected 293 T cells with UL82-myc and Rae1-hemagglutinine (Rae1-HA) or appropiate empty vectors as negative controls and performed a coimmunoprecipitation experiment, precipitating Rae1-HA with an HA antibody. The HA-tagged HCMV protein UL35, known to interact with UL82 (Liu & Cohen, 2016), was included as a positive control. In this overexpression context, UL82 coprecipitated with Rae1 and, as expected, with UL35 (Figure 5b). This suggests that UL82, as MHV68 ORF10, may influence mRNA export from the nucleus.

3 | DISCUSSION

Through millions of years of coevolution, herpesviruses have developed sophisticated strategies to secure lifelong persistence in their respective hosts. The diverse mechanisms by which HCMV controls its host are still incompletely understood; this bears the potential to discover novel, yet unanticipated, roles of cellular pathways for HCMV pathogenesis. The HCMV genome has a large coding potential, and in addition, many of its gene products exert multiple functions, often depending on the actual phase of the viral life cycle. The functional repertoire of the tegument protein UL82 is impressive, making it one of the essential viral gene products of this clinically relevant virus (Kalejta & Albright, 2020).

To further the exploration of the molecular mechanisms underlying the multiple functions of UL82, we have determined the crystal structure of this crucial viral protein in full length. On the basis of the three-dimensional structure, we identified structural homologs of UL82 from related herpesviruses and investigated, whether the structural similarities translate into functional ones. Closest matches with respect to the fold were the functional dUTPase BLLF3 from EBV and the ORF10 protein of MHV68 ORF10. This finding is in line with earlier sequence analyses, which predicted UL82 as well as MHV68 ORF10 to contain dUTPase motifs (Davison & Stow, 2005). Although the fold of two of the four domains of UL82 is very similar to that of the functional dUTPase BLLF3, close inspection of the putative active site in UL82 revealed that UL82 cannot bind dUTP. Moreover, we confirmed experimentally that UL82 does not display discernible dUTPase activity. We thus unequivocally clarified that dUTPase activity cannot be added to the functional repertoire of UL82.

The structural homology between UL82 and MHV68 ORF10 goes beyond their similarity in the dUTPase fold, suggesting that other functions may be preserved between these representatives of the betaherpesvirus and

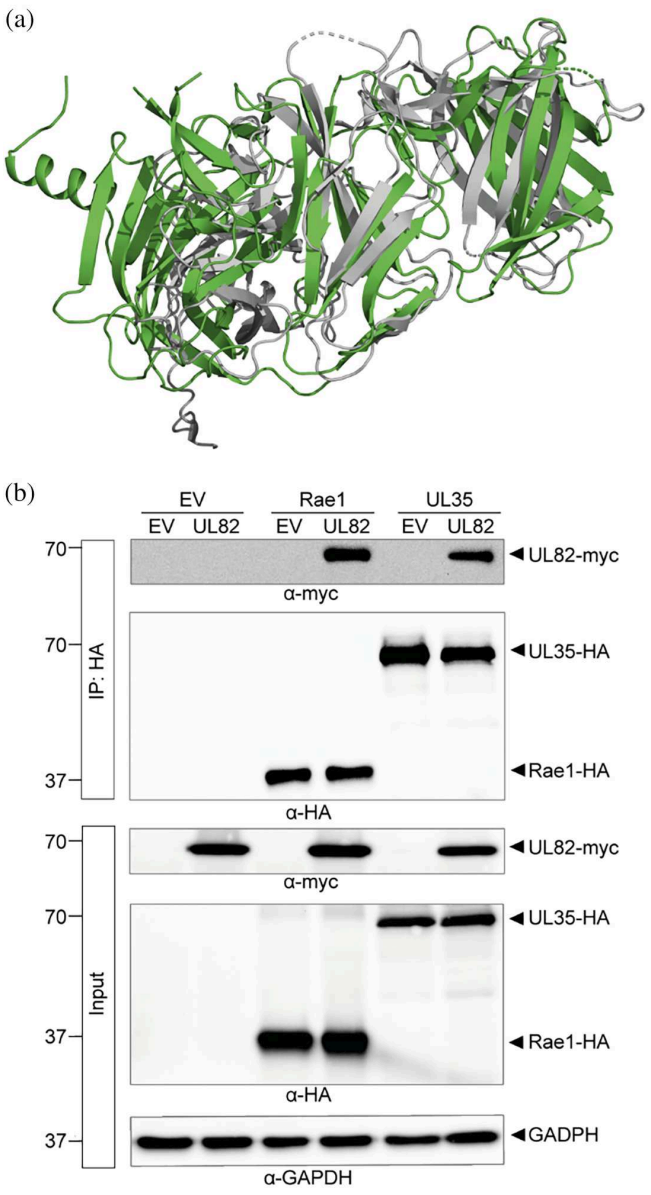

FIGURE 5 UL82 is a structural and also a potential functional homolog of ORF10 from Murine Herpesvirus 68 (MHV68) (a) Structural similarity of UL82 and ORF10. Superposition of a monomer of UL82 and ORF10 from MHV68 (PDB ID 7BYF) in cartoon depiction. UL82 is shown in green, ORF10 is shown in gray. Loops that are missing in the structures are shown as dotted lines. (b) Human cytomegalovirus (HCMV) UL82 and ribonucleic acid export 1 (Rae1) interact in 293 T cells. Lysates of 293 T cells transfected with an empty vector (EV) or plasmids encoding myc-tagged UL82 or HA-tagged Rae1 or UL35 were subjected to coimmunoprecipitation (IP) with an anti-HA antibody. IP samples and corresponding whole cell lysates were analyzed by immunoblotting with antibodies against the respective myc and hemagglutinine (HA) epitope tags. GAPDH served as loading control. PDB, protein data bank.

gammaherpesvirus subfamilies, respectively. MHV68 ORF10 was shown to directly interact with the mRNA export factor Rae1 (Feng et al., 2020), thereby selectively inhibiting nuclear export of a subset of cellular mRNAs (Gong et al., 2016). The functional consequences of this property for MHV68 replication are not yet clear. The ORF10 ortholog in the human oncogenic virus Kaposi's sarcoma-associated herpesvirus, which also interacts with Rae1, has been demonstrated to play a critical role for late viral gene expression (Gong et al., 2016). This prompted us to investigate whether the interaction seen for MHV68 ORF10 and Rae1 is preserved in UL82. Indeed, we found that UL82 coprecipitated with Rae1 upon transient expression in 293 T cells, which is the first time that an interaction of Rae1 with a protein of the *betaherpesviridae* is reported. It remains to be analyzed, whether the interaction of UL82 with Rae1 seen in our coimmunoprecipitation experiment is direct or is conveyed by a molecular intermediary. It may well be that RNA bridges the interaction of UL82 with Rae1. UL82 has previously been shown to interact with viral as well as cellular RNA, albeit the molecular details and functional consequences for HCMV infection were not revealed (Lenarcic et al., 2015). Whether the interaction between UL82 and Rae1 influences mRNA export of cellular and/or viral origin, and how it influences HCMV replication, is currently a subject of investigation.

The crystal structure of UL82 revealed a dimeric arrangement of UL82 that we could confirm in solution using purified protein as well as in human cells transiently expressing full-length UL82. We successfully identified residues that are critical for keeping the dimer of UL82 intact. We confirmed that insertion of the point mutations R66E and D522R disturb the dimerization interface, resulting in a mutant protein that is monomeric in solution and human cells. Opposed to our findings with the M35 tegument protein of murine CMV, which also presented as a dimer but whose expression was severely impaired when the dimer is disrupted (Schwanke et al., 2023), the UL82 dimerization mutant was expressed to levels as high as UL82-WT, which will allow continuing functional characterization.

From our crystal structure, we conclude that a dimeric status of UL82 hampers the interaction with STING as well as the binding of UL82 to Rb and its family members p107 and p130. The interaction with Rb is mediated by an LxCxD/E motif (Putta et al., 2022; Ramanujan et al., 2021), which corresponds to ^{216}LACSD^{220} in UL82. C218 in this motif is, at the same time, implied to be vital for the interaction of UL82 with STING (Nukui et al., 2020). In the dimer structure, the loop containing ^{216}LACSD^{220} is oriented such that the side chains of the motif are pointing toward the interior of the protein. To enable the side chains of the binding motif to interact with the target proteins, the loop would need to "flip" and present the relevant side chains to the surface of the protein. Such a big conformational

shift of the loop is sterically held up in the dimer and may only occur when UL82 becomes monomeric.

UL82 is known to be posttranslationally modified by phosphorylation at residue T223, which is located near the C-terminal end of the ^{216}LACSD^{220} motif. Phosphorylation of T223 has been implicated in the nuclear localization of UL82 (Shen et al., 2008). When T223 was mutated to D223, mimicking phosphorylation, UL82-T223D was not imported into the nucleus, suggesting a regulatory role for this residue (Shen et al., 2008). In our structure, the side chain of T223 is pointing toward D220 of the ^{216}LACSD^{220} motif, and it is conceivable that upon phosphorylation of T223, the newly introduced negative charge would prompt the aforementioned "flipping" of the loop to expose the motif for binding of Rb or C218 for the interaction with STING. This would explain how T223 phosphorylation can partake in counteracting STING-mediated signaling, albeit the residue itself might not be involved in the interaction between STING and UL82 (Nukui et al., 2020).

Taken together, the results presented here provide an excellent starting point for a plethora of future experiments to eventually explain how the tegument protein UL82 fulfills its multiple assignments during the life cycle of HCMV. On the basis of the first crystal structure of the UL82 dimer, we not only identified new regulatory features but also suggest yet another role of UL82. It will be interesting to see, whether UL82 indeed selectively controls RNA trafficking in the host cell and how this influences replication and persistence of the virus.

4 | MATERIALS AND METHODS

4.1 | Cloning, expression, and purification of recombinant proteins

The coding sequence corresponding to full-length UL82 (NCBI accession number CAA35356.1) was amplified by polymerase chain reaction (PCR) from genomic DNA from HCMV AD169 strain (NCBI accession number X17403.1) with primers 5′-GCG GAT CCA TGT CTC AGG CAT CGT CCT CGC C-3′ and 5′-GCC TCG AGC TAG ATG CGG GGT CGA CTG CGT GG-3′. The UL82 gene was cloned into a modified pFastBac vector (Invitrogen) with an N-terminal His_6-MBP-Tag followed by the TEV protease recognition site. The mutations R66E and D522R were introduced by megaprimer mutagenesis with primer pairs 5′-CGT ACC AAC ATA GAG GTG AGC GAG CCC TCG GTT CTC TGC TG-3′ & 5′-CAG CAG AGA ACC GAG GGC TCG CTC ACC TCT ATG TTG GTA CG-3′ and 5′-CTG CGC AGC GAC ATG GAC GGC AGA GTG CGT ACC GCG GCA GAC ATC-3′ & 5′-GAT GTC TGC CGC GGT ACG CAC TCT GCC GTC CAT GTC GCT GCG CAG-3′, respectively. A recombinant baculovirus was produced with the MultiBac system (Geneva Biotech) following the manufacturer's protocols. The coding sequence of full-length UL82 was PCR-amplified from the pFastBac vector with primers 5′-GCA TGG ATC CGT GCC ACC ATG TCT CAG GCA TCG TCC TC-3′ and 5′- CCA TGA ATT CCG ATG CGG GGT CGA CTG CGT-3′ and subsequently cloned into the pEF1/myc-His C vector (Invitrogen) via BamHI/EcoRI sites to generate pEF1 UL82-myc-His. UL35 was C-terminally epitope-tagged with 2×HA and cloned into the pEF1/myc-His C vector after amplification with the primers 5′-GCA TGG ATC CGC CAC CAT GGC CCA GGG ATC GCG AGC-3′ and 5′-CCA TGT TTA AAC AGC GGC CGC CTA TGC GTA GTC-3′ via BamHI/PmeI restriction sites, thereby removing the myc-His sequence to generate pEF1 UL35-HAHA.

The coding sequence for full-length Rae1 from *Homo sapiens* (NCBI accession number NP_003601.1) was cloned into a modified pcDNA3.1(+) vector containing a C-terminal HA-tag using the primers 5′-CAG GGA TCC ATG AGC CTG TTT GGA ACA ACC T-3′ and 5′-GCT CTC GAG CTT ATT CCT GGG CTT TAG CT-3′ to yield pcDNA-Rae1-HA. By PCR amplification with primers 5′-GCA TGG ATC CGC CAC CAT GAG CCT GTT TGG-3′ and 5′-CCA TGT TTA AAC TCA TCC AGC GTA ATC TG-3′, Rae1-HA was subcloned into the pEF1/myc-His C vector via BamHI/PmeI restriction sites as described for UL35, yielding pEF-Rae1-HA.

The coding sequence corresponding to the full-length dUTPase from *E. coli* (NCBI accession number WP_001298007) was cloned into a modified pGEX-4 T1 vector with an N-terminal His_6-MBP-Tag followed by the TEV protease recognition site instead of the GST-Tag using the primers 5′-GCA GGG ATC CAT GAA AAA AAT CGA CGT TAA GAT TCT GG-3′ and 5′-GCA CGT CGA CTC ACT GAC GAC CAG AGT GAC CAA AGC CGC C-3′.

For protein expression in *Sf9* (*Spodoptera frugiperda*) cells, 15 mL of the UL82 baculovirus was used to infect 1 L with 2×10^6 cells/mL, which were collected 72 h postinfection. Cells were lysed by sonication in lysis buffer containing 50 mM 4-(-2hydroxyethyl)-1-piperazineethanesulfonic acid (HEPES) (pH 7.5), 150 mM NaCl, 1 mM $MgCl_2$, 5% glycerol, 5 mM 2-mercaptoethanol, 0.5% Nonidet P-40, and 1 mM phenylmethylsulfonyl fluoride (PMSF). After centrifugation, the supernatant was incubated with 3 mL amylose resin (New England Biolabs) for 1.5 h. After incubation, the mixture was applied to gravity flow, washed with a buffer containing 50 mM HEPES (pH 7.5), 200 mM NaCl, 1 mM $MgCl_2$, 5% glycerol, and 5 mM 2-mercaptoethanol and eluted with the same buffer supplemented with 25 mM maltose. The eluted protein was

concentrated using ultrafiltration devices (Sartorius) and purified by size exclusion chromatography (SEC) on a Superdex 200 16/600 column (Cytiva) equilibrated with buffer containing 20 mM HEPES (pH 7.5), 150 mM NaCl, 1 mM $MgCl_2$, 5% glycerol, and 2 mM dithiothreitol (DTT). The peak fractions were pooled, concentrated, and flash-frozen in liquid nitrogen. All purification steps were performed at 4°C.

The *E. coli* dUTPase was expressed in *E. coli* BL21 (DE3) grown to an OD of 1.0 in terrific broth medium by induction with 0.2 mM IPTG overnight at 293°C. Cells were collected by centrifugation and lysed by sonication in a buffer containing 50 mM HEPES (pH 7.5), 150 mM NaCl, 1 mM $MgCl_2$, 5 mM 2-mercaptoethanol, 0.5% Nonidet P-40, 0.4 mg/mL hen egg-white lysozyme, and 1 mM PMSF. After centrifugation, the supernatant was incubated with 5 mL amylose resin (New England Biolabs) for 1.5 h. After incubation, the mixture was applied to a gravity flow column, washed with 50 mM HEPES (pH 7.5), 250 mM NaCl, 1 mM $MgCl_2$, and 5 mM 2-mercaptoethanol, and eluted with the same buffer supplemented with 25 mM maltose. The fractions containing protein were pooled and mixed with 3 mg TEV protease. After 2.5 h of incubation on ice, the mixture was diluted to a NaCl concentration of 50 mM and applied to a HiTrap Q HP column. The column was eluted with 50–800-mM NaCl. The fractions containing the dUTPase were collected, concentrated, and purified by SEC on a Superdex 200 10/300 column (Cytiva) in a buffer containing 20 mM HEPES (pH 7.5), 150 mM NaCl, 1 mM $MgCl_2$, and 2 mM DTT. The peak fractions were pooled, concentrated, and flash-frozen in liquid nitrogen. All purification steps were performed at 4°C.

4.2 | Crystallization

Crystals of native UL82 were obtained in sitting-drop vapor diffusion experiments. For the droplets, 1 µL with 13 mg/mL MBP-UL82 were mixed with 1 µL reservoir solution containing 0.1 M MES (pH 6.5), 0.2 M $MgCl_2$, and 72.5 g/L PEG4000. The droplets were equilibrated against 200 µL reservoir at 18°C. Crystals were flash-cooled in liquid nitrogen in reservoir solution supplemented with 29% PEG400. For heavy atom derivatization, crystals were incubated in reservoir solution containing 0.1 mM thiomersal for 16 h. Cryoprotection of derivative crystals was performed as for native crystals.

4.3 | Data collection and processing

Complete diffraction data to a resolution of 2.7 Å were collected from a native crystal at EMBL beamline P13 at PETRAIII (DESY, Hamburg, Germany), measured at 100 K and a wavelength of 0.978565 Å. From a crystal derivatized with thiomersal, five data sets were measured to a resolution of 3.1 Å at a wavelength of 1.00522 Å at beamline EMBL beamline P13. Data were processed with XDS and scaled with XScale (Kabsch, 2010).

4.4 | Structure solution and refinement

The crystal structure was solved by the single anomalous dispersion method using the CRANK2 pipeline (Skubak & Pannu, 2013) on the merged derivative data. The resulting model was iteratively refined against the native data using Phenix.refine (Liebschner et al., 2019). After each refinement cycle, the structure was manually adjusted in COOT (Emsley et al., 2010). For the preparation of images displaying structural data, PyMOL (The PyMOL Molecular Graphics System, Version 2.5.2., Schrödinger, LLC) was used. X-ray data collection and refinement statistics are summarized in Table 1. The atomic coordinates and structure factors of UL82 have been deposited in the Protein Data Bank (PDB entry 8QDO).

4.5 | Analytical size exclusion chromatography

Hundred microliters containing either 100, 10, or 1 µmol/L of either MBP-UL82-WT or MBP-UL82-R66E/D522R were applied to an S200 10/300 size exclusion column (GE Healthcare). The column was equilibrated with a buffer containing 20 mM HEPES (pH 7.5), 150 mM NaCl, 1 mM $MgCl_2$, 5% glycerol, and 2 mM DTT. The absorption chromatograms at 280 nm were collected at a flow rate of 0.3 mL/min and a temperature of 7°C.

4.6 | dUTPase activity assay

Kinetics of dUTP hydrolysis into dUMP and pyrophosphate were determined by mixing equal volumes of 100 nM protein in activity buffer (1 mM HEPES [pH 7.5], 5 mM $MgCl_2$, 150 mM KCl, 80 µM phenol red) with 120 µM dUTP in activity buffer in a stopped-flow unit, for final protein and dUTP concentrations of 50 nM and 60 µM, respectively. Proton release during dUTP hydrolysis was monitored continuously for 450 s via pH-dependent changes in the absorption of phenol red at a wavelength of 559 nm. All kinetic measurements were performed at 25°C using a HiTech Scientific SF-61SX2 Stopped-Flow System (TgK Scientific, Bradford-on-Avon, UK). Initial velocities were determined from the slope of the first 10% of the resulting progress curves. Turnover

frequencies were derived directly from both initial velocities and plateaus of the progress curves or were approximated using a mean conversion factor obtained from the direct derivation.

4.7 | Cell culture, native PAGE, immunoprecipitation

Human embryonic kidney 293 T cells (CRL-3216) were obtained from ATCC (Manassas, VA, USA) and cultured in Dulbecco's modified Eagle's medium (high glucose) supplemented with 10% fetal calf serum and 1% penicillin/streptomycin at 37°C with 5% CO_2. For native PAGE, 1.5×10^5 293 T cells were seeded in a 24-well format and transfected the following day with 500 ng DNA of either the empty vector (pEF1/myc-His C), pEF-UL82-myc-His WT, or the pEF-UL82-myc-His R66E/D522R mutant, using 2 μL FuGENE HD (Promega) in 30 μL Opti-MEM/well. Cells were lysed 20 h posttransfection in 70 μL lysis buffer (20 mM Tris–HCl [pH 7.5], 100 mM NaCl, 1 mM EDTA, 1% Triton X-100, 1 g/L sodium dodecyl sulfate [SDS], 5 g/L sodium deoxycholate [DOC]), freshly supplemented with protease inhibitors (Roche), rotating for 1 h at 4°C. Cell debris was pelleted by centrifugation and the supernatant was mixed with 2× native loading buffer (125 mM Tris–HCl [pH 6.8], 60% glycerol, 2 g/L bromophenol blue). The native gel was composed of a 5% polyacrylamide stacking gel (5% acrylamide/bis-acrylamide [37.5:1], 375 mM Tris–HCl [pH 8.8], 0.033% ammonium persulfate [APS], 0.133% tetramethylethylenediamine [TEMED]) and a 7.5% separating gel (7.5% acrylamide/bis-acrylamide [37.5:1], 125 mM Tris–HCl [pH 6.8], 0.075% APS, 0.2% TEMED) and was prerun at 4°C at 40 mA for 30 min with Tris–glycine buffer (25 mM Tris–base [pH 8.3], 192 mM glycine) as anode buffer and Tris–glycine buffer supplemented with 2 g/L DOC as cathode buffer. Upon completion of the prerun, the used cathode buffer was replaced with fresh cathode buffer, samples were loaded, and the native PAGE was run at 4°C first at 6 mA, until proteins had passed the stacking gel, then at 10 mA. For the corresponding SDS-PAGE, supernatant was mixed with 4× SDS loading buffer (250 mM Tris–HCl [pH 6.8], 40% glycerol, 10% 2-mercaptoethanol, 80 g/L SDS, 0.4 g/L bromophenol blue) and loaded onto a gel composed of a 5% polyacrylamide stacking gel (5% acrylamide/bis-acrylamide [37.5:1], 375 mM Tris–HCl [pH 8.8], 1 g/L SDS, 0.075% APS, 0.2% TEMED) and a 10% polyacrylamide separating gel (10% acrylamide/bis-acrylamide [37.5:1], 125 mM Tris–HCl [pH 6.8], 1 g/L SDS, 0.075% APS, 0.2% TEMED) which was run in Tris–glycine buffer at room temperature (RT). Proteins were blotted on a 0.45 μm nitrocellulose membrane (Cytiva) in a wet blot system in Tris–glycine transfer buffer (25 mM Tris–base [pH 8.3], 192 mM glycine, 0.5 g/L SDS, 20% methanol) for 1 h at 350 mA at 4°C. The membrane of the native PAGE was then incubated in fixation solution (40% ethanol, 7% acetic acid, 3% glycerol) for 15 min at RT and washed three times in Tris buffer (20 mM Tris–base [pH 8.0], 150 mM NaCl) with 0.1% Tween 20 (TBS-T). Both membranes were then blocked with 5% bovine serum albumine in TBS-T (blocking solution) for 1 h at RT before being incubated with anti-myc (cat. no. 2276, Cell Signaling Technology) or anti-glyceraldehyde-3-phosphate dehydrogenase (GAPDH) (cat. no. 2118, Cell Signaling Technology) primary antibodies diluted in blocking solution at 4°C overnight. Then, membranes were washed three times in TBS-T and, respectively, incubated with HRP-coupled anti-mouse (cat. no. 115–035-068, Dianova) or anti-rabbit (cat. no. 111–035-045, Dianova) secondary antibodies diluted in blocking solution for 1 h at RT. Finally, membranes were again washed three times in TBS-T before being developed with Pierce ECL substrate (Thermo Fisher Scientific) and imaged on a ChemoStar ECL Imager (INTAS).

For coimmunoprecipitation experiments, 8.5×10^5 293 T cells were seeded in a 6-well format and transfected the following day with 3 μg of total DNA of either only the empty vector pEF1/myc-His C or in combination (in 1:1 ratio) with the plasmids pEF-UL82-myc-His, pEF-Rae1-HA, or pEF-UL35-HAHA complexed with 12 μL Polyethylenimine (Polysciences) in a total of 200 μL PBS per well. 20 h later, cells were lysed in 500 μL IP lysis buffer (20 mM Tris–HCl [pH 7.5], 150 mM NaCl, 1% Nonidet P-40, 2.5 g/L DOC, 1 g/L SDS) with freshly added protease inhibitors. Ten percentage of the whole cell lysate was used as the input control, and the remaining sample was precleared with protein A agarose beads (Repligen IPA300S) for 1 h. The cleared lysates were subjected to immunoprecipitation with an anti-HA antibody (cat.no. 3724, Cell Signaling Technology) overnight at 4°C followed by incubation for 1 h with protein A agarose beads. Beads were washed seven times with IP lysis buffer and bound protein was eluted in 2× SDS loading buffer. Input and IP fraction were analyzed by SDS-PAGE immunoblotting with anti-myc and anti-GAPDH antibodies as described above or with an HRP-coupled anti-HA antibody (clone 3F10, Roche).

AUTHOR CONTRIBUTIONS

Jan Eberhage: Formal analysis; investigation; validation; visualization. **Ian P. Bresch:** Investigation; data curation. **Ramya Ramani:** Data curation; formal analysis; investigation; visualization. **Niklas Viohl:** Data curation; formal analysis; investigation; visualization. **Thalea Buchta:** Data curation; formal analysis; visualization;

investigation. **Christopher L. Rehfeld:** Investigation. **Petra Hinse:** Investigation. **Thomas F. Reubold:** Data curation; formal analysis; investigation; visualization; writing – original draft. **Melanie M. Brinkmann:** Conceptualization; funding acquisition; resources; supervision; writing – original draft; writing – review and editing. **Susanne Eschenburg:** Conceptualization; funding acquisition; resources; supervision; writing – review and editing; writing – original draft.

ACKNOWLEDGMENTS

We thank Martin Messerle and Eva-Maria Borst for providing the viral DNA template of HCMV strain AD169 and David von Stetten for support during remote data collection. The project was supported by the Deutsche Forschungsgemeinschaft (DFG, German Research Foundation) under Germany's Excellence Strategy—EXC 2155 'RESIST'—Project ID 390874280. Ian P. Bresch was a graduate student in the MD/PhD program Molecular Medicine of the Hannover Biomedical Research School (HBRS). Ramya Ramani, Thalea Buchta, and Melanie M. Brinkmann were funded by the Deutsche Forschungsgemeinschaft in the framework of Research Unit FOR5200 DEEP-DV (443644894) through project BR 3432/7-1 and the Life Science Foundation. Open Access funding enabled and organized by Projekt DEAL.

CONFLICT OF INTEREST STATEMENT

The authors declare no competing interests.

ORCID

Susanne Eschenburg https://orcid.org/0000-0002-7422-618X

REFERENCES

Azevedo LS, Pierrotti LC, Abdala E, Costa SF, Strabelli TMV, Campos SV, et al. Cytomegalovirus infection in transplant recipients. Clinics (Sao Paulo). 2015;70(7):515–23. https://doi.org/10.6061/clinics/2015(07)09

Berry R, Watson GM, Jonjic S, Degli-Esposti MA, Rossjohn J. Modulation of innate and adaptive immunity by cytomegaloviruses. Nat Rev Immunol. 2020;20(2):113–27. https://doi.org/10.1038/s41577-019-0225-5

Bogdanow B, Gruska I, Mühlberg L, Protze J, Hohensee S, Vetter B, et al. Spatially resolved protein map of intact human cytomegalovirus virions. Nat Microbiol. 2023;8(9):1732–47. https://doi.org/10.1038/s41564-023-01433-8

Cedergren-Zeppezauer ES, Larsson G, Nyman PO, Dauter Z, Wilson KS. Crystal structure of a dUTPase. Nature. 1992;355(6362):740–3. https://doi.org/10.1038/355740a0

Cho S-Y, Lee D-G, Kim H-J. Cytomegalovirus infections after hematopoietic stem cell transplantation: current status and future immunotherapy. Int J Mol Sci. 2019;20(11):2666. https://doi.org/10.3390/ijms20112666

Coppola T, Mangold JF, Cantrell S, Permar SR. Impact of maternal immunity on congenital cytomegalovirus birth prevalence and infant outcomes: a systematic review. Vaccine. 2019;7(4):129. https://doi.org/10.3390/vaccines7040129

Davison AJ, Dolan A, Akter P, Addison C, Dargan DJ, Alcendor DJ, et al. The human cytomegalovirus genome revisited: comparison with the chimpanzee cytomegalovirus genome. J Gen Virol. 2003;84(Pt 1):17–28. https://doi.org/10.1099/vir.0.18606-0

Davison AJ, Stow ND. New genes from old: redeployment of dUTPase by herpesviruses. J Virol. 2005;79(20):12880–92. https://doi.org/10.1128/JVI.79.20.12880-12892.2005

Dietrich ML, Schieffelin JS. Congenital cytomegalovirus infection. Ochsner J. 2019;19(2):123–30. https://doi.org/10.31486/toj.18.0095

Dunn W, Chou C, Li H, Hai R, Patterson D, Stolc V, et al. Functional profiling of a human cytomegalovirus genome. Proc Natl Acad Sci U S A. 2003;100(24):14223–8. https://doi.org/10.1073/pnas.2334032100

Emsley P, Lohkamp B, Scott WG, Cowtan K. Features and development of Coot. Acta Crystallogr D Biol Crystallogr. 2010;66:486–501.

Feng H, Tian H, Wang Y, Zhang Q, Lin N, Liu S, et al. Molecular mechanism underlying selective inhibition of mRNA nuclear export by herpesvirus protein ORF10. Proc Natl Acad Sci U S A. 2020;117(43):26719–27. https://doi.org/10.1073/pnas.2007774117

Fowler KB, Boppana SB. Congenital cytomegalovirus infection. Semin Perinatol. 2018;42(3):149–54. https://doi.org/10.1053/j.semperi.2018.02.002

Fu Y-Z, Su S, Gao Y-Q, Wang P-P, Huang Z-F, Hu M-M, et al. Human cytomegalovirus tegument protein UL82 inhibits STING-mediated signaling to evade antiviral immunity. Cell Host Microbe. 2017;21(2):231–43. https://doi.org/10.1016/j.chom.2017.01.001

Gatherer D, Seirafian S, Cunningham C, Holton M, Dargan DJ, Baluchova K, et al. High-resolution human cytomegalovirus transcriptome. Proc Natl Acad Sci U S A. 2011;108(49):19755–60. https://doi.org/10.1073/pnas.1115861108

Goderis J, De Leenheer E, Smets K, Van Hoecke H, Keymeulen A, Dhooge I. Hearing loss and congenital CMV infection: a systematic review. Pediatrics. 2014;134(5):972–82. https://doi.org/10.1542/peds.2014-1173

Gong D, Kim YH, Xiao Y, Du Y, Xie Y, Lee KK, et al. A herpesvirus protein selectively inhibits cellular mRNA nuclear export. Cell Host Microbe. 2016;20(5):642–53. https://doi.org/10.1016/j.chom.2016.10.004

Griffiths P, Reeves M. Pathogenesis of human cytomegalovirus in the immunocompromised host. Nat Rev Microbiol. 2021;19(12):759–73. https://doi.org/10.1038/s41579-021-00582-z

Hofmann H, Sindre H, Stamminger T. Functional interaction between the pp71 protein of human cytomegalovirus and the PML-interacting protein human Daxx. J Virol. 2002;76(11):5769–83. https://doi.org/10.1128/jvi.76.11.5769-5783.2002

Holm L. Dali server: structural unification of protein families. Nucleic Acids Res. 2022;50(W1):W210–5. https://doi.org/10.1093/nar/gkac387

Hwang J, Kalejta RF. Proteasome-dependent, ubiquitin-independent degradation of Daxx by the viral pp71 protein in human cytomegalovirus-infected cells. Virology. 2007;367(2):334–8. https://doi.org/10.1016/j.virol.2007.05.037

Kabsch W. XDS. Acta Crystallogr D Biol Crystallogr. 2010;66:125–32.

Kalejta RF. Human cytomegalovirus pp71: a new viral tool to probe the mechanisms of cell cycle progression and oncogenesis controlled by the retinoblastoma family of tumor suppressors. J Cell Biochem. 2004;93(1):37–45. https://doi.org/10.1002/jcb.20177

Kalejta RF. Tegument proteins of human cytomegalovirus. Microbiol Mol Biol Rev. 2008;72(2):249–65, table of contents. https://doi.org/10.1128/MMBR.00040-07

Kalejta RF, Albright ER. Expanding the known functional repertoire of the human cytomegalovirus pp71 protein. Front Cell Infect Microbiol. 2020;10:95. https://doi.org/10.3389/fcimb.2020.00095

Kalejta RF, Bechtel JT, Shenk T. Human cytomegalovirus pp71 stimulates cell cycle progression by inducing the proteasome-dependent degradation of the retinoblastoma family of tumor suppressors. Mol Cell Biol. 2003;23(6):1885–95. https://doi.org/10.1128/MCB.23.6.1885-1895.2003

Kalejta RF, Shenk T. Proteasome-dependent, ubiquitin-independent degradation of the Rb family of tumor suppressors by the human cytomegalovirus pp71 protein. Proc Natl Acad Sci U S A. 2003a;100(6):3263–8. https://doi.org/10.1073/pnas.0538058100

Kalejta RF, Shenk T. The human cytomegalovirus UL82 gene product (pp71) accelerates progression through the G1 phase of the cell cycle. J Virol. 2003b;77(6):3451–9. https://doi.org/10.1128/jvi.77.6.3451-3459.2003

Krissinel E, Henrick K. Inference of macromolecular assemblies from crystalline state. J Mol Biol. 2007;372(3):774–97. https://doi.org/10.1016/j.jmb.2007.05.022

Lee JO, Russo AA, Pavletich NP. Structure of the retinoblastoma tumour-suppressor pocket domain bound to a peptide from HPV E7. Nature. 1998;391(6670):859–65. https://doi.org/10.1038/36038

Lenarcic EM, Ziehr BJ, Moorman NJ. An unbiased proteomics approach to identify human cytomegalovirus RNA-associated proteins. Virology. 2015;481:13–23. https://doi.org/10.1016/j.virol.2015.02.008

Liebschner D, Afonine PV, Baker ML, Bunkoczi G, Chen VB, Croll TI, et al. Macromolecular structure determination using X-rays, neutrons and electrons: recent developments in Phenix. Acta Crystallogr D Struct Biol. 2019;75(Pt 10):861–77. https://doi.org/10.1107/S2059798319011471

Liu X, Cohen JI. Epstein-Barr virus (EBV) tegument protein BGLF2 promotes EBV reactivation through activation of the p38 mitogen-activated protein kinase. J Virol. 2016;90(2):1129–38. https://doi.org/10.1128/JVI.01410-15

Mustafi D, Bekesi A, Vertessy BG, Makinen MW. Catalytic and structural role of the metal ion in dUTP pyrophosphatase. Proc Natl Acad Sci U S A. 2003;100(10):5670–5. https://doi.org/10.1073/pnas.1031504100

Njue A, Coyne C, Margulis AV, Wang D, Marks MA, Russell K, et al. The role of congenital cytomegalovirus infection in adverse birth outcomes: a review of the potential mechanisms. Viruses. 2020;13(1):20. https://doi.org/10.3390/v13010020

Nobre LV, Nightingale K, Ravenhill BJ, Antrobus R, Soday L, Nichols J, et al. Human cytomegalovirus interactome analysis identifies degradation hubs, domain associations and viral protein functions. Elife. 2019;8:e49894. https://doi.org/10.7554/eLife.49894

Nukui M, Roche KL, Jia J, Fox PL, Murphy EA. Protein S-Nitrosylation of human cytomegalovirus pp71 inhibits its ability to limit STING antiviral responses. J Virol. 2020;94(17):e00033-20. https://doi.org/10.1128/JVI.00033-20

Phillips SL, Bresnahan WA. Identification of binary interactions between human cytomegalovirus virion proteins. J Virol. 2011;85(1):440–7. https://doi.org/10.1128/JVI.01551-10

Putta S, Alvarez L, Lüdtke S, Sehr P, Müller GA, Fernandez SM, et al. Structural basis for tunable affinity and specificity of LxCxE-dependent protein interactions with the retinoblastoma protein family. Structure. 2022;30(9):1340–1353.e3. https://doi.org/10.1016/j.str.2022.05.019

Ramanujan A, Bansal S, Guha M, Pande NT, Tiwari S. LxCxD motif of the APC/C coactivator subunit FZR1 is critical for interaction with the retinoblastoma protein. Exp Cell Res. 2021;404(2):112632. https://doi.org/10.1016/j.yexcr.2021.112632

Rawlinson WD, Boppana SB, Fowler KB, Kimberlin DW, Lazzarotto T, Alain S, et al. Congenital cytomegalovirus infection in pregnancy and the neonate: consensus recommendations for prevention, diagnosis, and therapy. Lancet Infect Dis. 2017;17(6):e177–88. https://doi.org/10.1016/S1473-3099(17)30143-3

Razonable RR, Humar A. Cytomegalovirus in solid organ transplant recipients-guidelines of the American Society of Transplantation infectious diseases Community of Practice. Clin Transplant. 2019;33(9):e13512. https://doi.org/10.1111/ctr.13512

Saffert RT, Kalejta RF. Inactivating a cellular intrinsic immune defense mediated by Daxx is the mechanism through which the human cytomegalovirus pp71 protein stimulates viral immediate-early gene expression. J Virol. 2006;80(8):3863–71. https://doi.org/10.1128/JVI.80.8.3863-3871.2006

Saffert RT, Kalejta RF. Human cytomegalovirus gene expression is silenced by Daxx-mediated intrinsic immune defense in model latent infections established in vitro. J Virol. 2007;81(17):9109–20. https://doi.org/10.1128/JVI.00827-07

Schierling K, Stamminger T, Mertens T, Winkler M. Human cytomegalovirus tegument proteins ppUL82 (pp71) and ppUL35 interact and cooperatively activate the major immediate-early enhancer. J Virol. 2004;78(17):9512–23. https://doi.org/10.1128/JVI.78.17.9512-9523.2004

Schwanke H, Gonçalves Magalhães V, Schmelz S, Wyler E, Hennig T, Günther T, et al. The cytomegalovirus M35 protein directly binds to the interferon-β enhancer and modulates transcription of Ifnb1 and other IRF3-driven genes. J Virol. 2023;97(6):e0040023. https://doi.org/10.1128/jvi.00400-23

Shen W, Westgard E, Huang L, Ward MD, Osborn JL, Chau NH, et al. Nuclear trafficking of the human cytomegalovirus pp71 (ppUL82) tegument protein. Virology. 2008;376(1):42–52. https://doi.org/10.1016/j.virol.2008.03.007

Skubak P, Pannu NS. Automatic protein structure solution from weak X-ray data. Nat Commun. 2013;4:2777. https://doi.org/10.1038/ncomms3777

Stern-Ginossar N, Weisburd B, Michalski A, Le VTK, Hein MY, Huang S-X, et al. Decoding human cytomegalovirus. Science. 2012;338(6110):1088–93. https://doi.org/10.1126/science.1227919

Tarbouriech N, Buisson M, Seigneurin J-M, Cusack S, Burmeister WP. The monomeric dUTPase from Epstein-Barr virus mimics trimeric dUTPases. Structure. 2005;13(9):1299–310. https://doi.org/10.1016/j.str.2005.06.009

To A, Bai Y, Shen A, Gong H, Umamoto S, Lu S, et al. Yeast two hybrid analyses reveal novel binary interactions between human cytomegalovirus-encoded virion proteins. PloS One. 2011;6(4):e17796. https://doi.org/10.1371/journal.pone.0017796

Trgovcich J, Cebulla C, Zimmerman P, Sedmak DD. Human cytomegalovirus protein pp71 disrupts major histocompatibility complex class I cell surface expression. J Virol. 2006;80(2):951–63. https://doi.org/10.1128/JVI.80.2.951-963.2006

Tye BK, Nyman PO, Lehman IR, Hochhauser S, Weiss B. Transient accumulation of Okazaki fragments as a result of uracil incorporation into nascent DNA. Proc Natl Acad Sci U S A. 1977;74(1):154–7. https://doi.org/10.1073/pnas.74.1.154

Varnum SM, Streblow DN, Monroe ME, Smith P, Auberry KJ, Pasa-Tolic L, et al. Identification of proteins in human cytomegalovirus (HCMV) particles: the HCMV proteome. J Virol. 2004;78(20):10960–6. https://doi.org/10.1128/JVI.78.20.10960-10966.2004

Yang R, Zhang R, Zhang Y, Huang Y, Liang H, Gui G, et al. Risk factors analysis for human cytomegalovirus viremia in donor +/recipient+ hematopoietic stem cell transplantation. Lab Med. 2020;51(1):74–9. https://doi.org/10.1093/labmed/lmz030

Yu X, Shah S, Lee M, Dai W, Lo P, Britt W, et al. Biochemical and structural characterization of the capsid-bound tegument proteins of human cytomegalovirus. J Struct Biol. 2011;174(3):451–60. https://doi.org/10.1016/j.jsb.2011.03.006

Yu D, Silva MC, Shenk T. Functional map of human cytomegalovirus AD169 defined by global mutational analysis. Proc Natl Acad Sci U S A. 2003;100(21):12396–401. https://doi.org/10.1073/pnas.1635160100

Zuhair M, Smit GSA, Wallis G, Jabbar F, Smith C, Devleesschauwer B, et al. Estimation of the worldwide seroprevalence of cytomegalovirus: a systematic review and meta-analysis. Rev Med Virol. 2019;29(3):e2034. https://doi.org/10.1002/rmv.2034

SUPPORTING INFORMATION

Additional supporting information can be found online in the Supporting Information section at the end of this article.

How to cite this article: Eberhage J, Bresch IP, Ramani R, Viohl N, Buchta T, Rehfeld CL, et al. Crystal structure of the tegument protein UL82 (pp71) from human cytomegalovirus. Protein Science. 2024;33(3):e4915. https://doi.org/10.1002/pro.4915